Letter

# Continuum-electron interferometry for enhancement of photoelectron circular dichroism and measurement of bound, free, and mixed contributions to chiral response

R. Esteban Goetz,[1,*] Alexander Blech,[2] Corbin Allison,[1] Christiane P. Koch,[2] and Loren Greenman[1,†]
[1]J. R. Macdonald Laboratory, Department of Physics, Kansas State University, Manhattan, Kansas 66506, USA.
[2]Dahlem Center for Complex Quantum Systems and Fachbereich Physik, Freie Universität Berlin, Arnimallee 14, D-14195 Berlin, Germany

(Received 15 November 2023; revised 18 May 2025; accepted 25 July 2025; published 14 August 2025)

We develop photoelectron interferometry based on laser-assisted extreme ultraviolet ionization for flexible and robust control of photoelectron circular dichroism in randomly oriented chiral molecules. A comb of XUV photons ionizes a sample of chiral molecules in the presence of a time-delayed infrared or visible laser pulse promoting interferences between components of the XUV-ionized photoelectron wave packet. In striking contrast to multicolor phase control schemes relying on pulse shaping techniques, the magnitude of the resulting chiral signal is here controlled by the time delay between the XUV and laser pulses. Furthermore, we show that the relative polarization configurations of the XUV and IR fields allow for disentangling the contributions of bound and continuum states to the chiral response. Our proposal provides a simple, robust, and versatile tool for the control of photoelectron circular dichroism and experimentally feasible protocol for probing the individual contributions of bound and continuum states to the photoelectron circular dichroism in a time-resolved manner.

DOI: 10.1103/8f7h-6nfc

Chirality, the property of a molecule to be nonsuperposable with its mirror image [1], is a ubiquitous property in nature with profound effects on many fundamental chemical and physical processes. Photoelectron circular dichroism (PECD) is a signature of chirality and designates the relatively strong effect whereby randomly oriented chiral molecules ionize asymmetrically for left- and right-circularly polarized light [2]. The strength of PECD has led to its use to observe chirality in molecules [3–19] and turned it into a practical tool for, e.g., measuring enantiomeric excess [6,16,17]. Since PECD probes molecular chirality with electric fields only, it is a natural candidate for coherent control, from pump-probe spectroscopy [13,20] to more advanced pulse shaping [21] or carrier-envelope phase control [22]. Coherent control techniques also allow for measuring PECD within a single experiment, not requiring polarization reversal, when using bichromatic fields [23,24]. PECD can be enhanced by interference, either between ionization pathways in resonantly enhanced multiphoton ionization [21] or by Fano interference near a continuum resonance [25]. While these techniques attest to the versatility of PECD, it is not yet clear what determines the values that PECD can take for a given molecule [26] nor how the chirality of bound or continuum states reflects in the PECD. Furthermore, coherent control schemes aiming at large enhancements of the PECD such as the shaped ionization pulses we have previously suggested [21] require challenging generation of and control over the spectral coherence of multicolor ultraviolet laser fields.

In this Letter, we propose a flexible, yet robust implementation of coherent control of PECD in randomly oriented molecules that neither requires shaping circularly polarized XUV laser sources, a formidable experimental challenge, nor relies on the accurate calculation of electronically excited states in chiral molecules, out of reach for even the most advanced *ab initio* theories. Rather, it leverages the RABBITT (reconstruction of attosecond beating by interference of two-photon transitions) technique [27,28], a versatile interferometric approach that has been implemented in many experimental laboratories [29–31]. The necessary circularly polarized XUV fields have been synthesized [32,33] and used in PECD experiments recently [34]. In contrast to the shaping of photoelectron wave packets in strong-field above-threshold ionization [15], our pathway interference operates in the perturbative regime of light-matter interaction. This opens the way to probing spectroscopically bound and continuum contributions to PECD and thus to quantify how short- and long-range interactions reflect in a chiral observable.

Using CHBrClF as a prototypical chiral molecule [35,36], we explain how promoting interferences in the continuum in a controlled manner results in precise control of PECD after XUV ionization in the presence of a time-delayed IR field. Rather than relying on multiple resonantly enhanced multiphoton ionization and multicolor pulse shaping techniques to control PECD [21], control here is achieved by adjusting the time delay between the XUV comb and IR field or by varying the IR pulse duration. Changing the polarization configuration of the pulses with optimized delay and IR duration allows for revealing the chiral contributions of different states.

*Present address: Department of Physics, AMO Theory Center, University of Connecticut, 196A Auditorium Road, Unit 3046, Storrs, Connecticut 06269, USA.
†Contact author: lgreenman@phys.ksu.edu

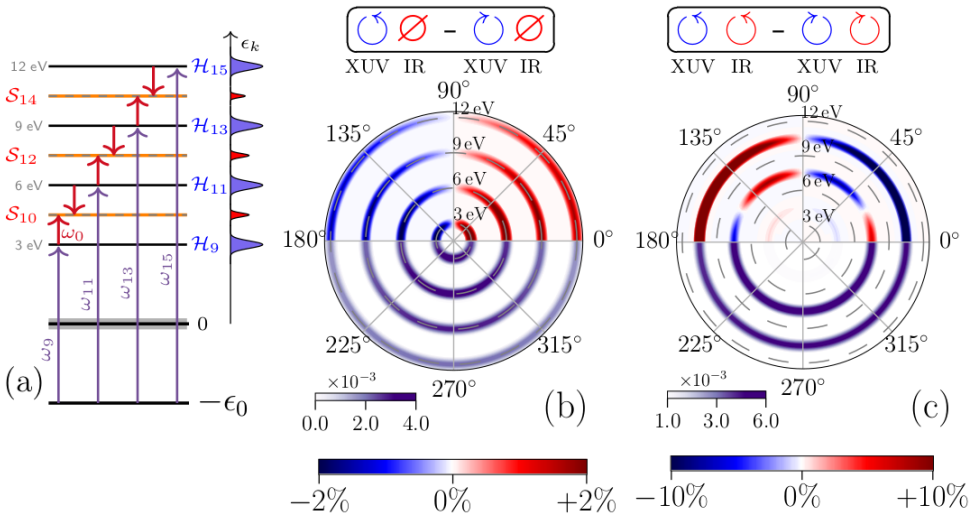


FIG. 1. RABBITT scheme for measuring PECD: (a) A comb of XUV harmonics ionizes a chiral molecule with ionization potential $\epsilon_0$, generating the harmonics $\mathcal{H}_{2q+1}$. (b) PECD (upper hemisphere) and PAD (lower hemisphere) resulting from single-photon ionization by the XUV comb in the absence of the IR field. (c) PECD and PAD in the presence of the IR field. PECD is given in percentage of peak intensity in the PAD, polarization configurations are depicted by the blue (XUV) and red (IR) arrows, and PADs are shown for left circular polarization.

The photoionization dynamics is described within the fixed-nuclei and nonrelativistic dipole approximations. The time-dependent Schrödinger equation reads

$$i\frac{\partial}{\partial t}\left|\Psi^N_{\gamma_\mathcal{R}}(t)\right\rangle = \left[\hat{\mathsf{H}}_0 + \sum_{\mu,\mu'}\mathcal{D}^{(1)*}_{\mu,\mu'}(\gamma_\mathcal{R})\,E_{\mu'}(t)\,\hat{\mathsf{r}}_\mu\right]\left|\Psi^N_{\gamma_\mathcal{R}}(t)\right\rangle, \tag{1a}$$

with $\hat{\mathsf{H}}_0$ the field-free Hamiltonian, $\gamma_\mathcal{R}$ the Euler angles defining the orientation of the molecular frame, $\mathcal{R}$, with respect to the laboratory frame $\mathcal{R}'$, $\mathcal{D}^{(1)}_{\mu,\mu'}(\gamma_\mathcal{R})$ the elements of the Wigner rotation matrix, $E_\mu(t)$ the electric field component along the spherical unit vector $\mathbf{e}_\mu$, with $\mu = \pm 1, 0$, and finally, $\hat{\mathsf{r}}_\mu$ the component of the position in the direction of $\mathbf{e}_\mu$. In $\mathcal{R}'$, the electric field is a superposition of the XUV comb and IR, resp. visible field,

$$\mathbf{E}(t) = \sum_n^{N_p}\mathbf{E}^{(\mathrm{XUV})}_n(t) + \mathbf{E}^{(\mathrm{IR/VIS})}(t-\tau_{\mathrm{IR/VIS}}), \tag{1b}$$

with $N_p$ the number of pulses in the XUV comb, and

$$\mathbf{E}^{(\mathrm{XUV})}_n(t) = h_n(t-\tau_n)\mathrm{Re}\{\mathrm{E}_{n,0}\,e^{-i(\omega_n(t-\tau_n)+\tilde{\phi}_n)}\,\mathbf{e}_{\mathrm{XUV}}\},$$

where $n = 2q+1$ with $q$ an integer; i.e., the XUV frequencies are odd multiples of the fundamental, $\omega_0$, $\omega_{2q+1} = (2q+1)\omega_0$. $h_n(\cdot)$ is a Gaussian function and $\mathbf{e}_{\mathrm{XUV}}$ the spherical unit vector describing circularly left ($\mathbf{e}_{-1} = (\mathbf{e}_x - i\mathbf{e}_y)/\sqrt{2}$), right ($\mathbf{e}_{+1} = -(\mathbf{e}_x + i\mathbf{e}_y)/\sqrt{2}$), and linear ($\mathbf{e}_0 = \mathbf{e}_z$) polarization of the radiation field. Here, $\tau_n$ describes the inherent chirp if the various XUV components are temporally delayed [37,38]. IR and visible pulses are analogously defined with $h_{\mathrm{IR/VIS}}(t-\tau_{\mathrm{IR/VIS}})$ and $\omega_{\mathrm{IR/VIS}}$, and $\tau_{\mathrm{IR/VIS}}$ describes the delay between the IR/VIS and XUV field. We explore two cases. First, the frequency $\omega_{\mathrm{IR}}$ is identical with the fundamental $\omega_0$ ($\omega_{\mathrm{IR}} = \omega_0 = 1.5\,\mathrm{eV}$) to control PECD at the sidebands [cf. Fig. 1(a)]. Second, the frequency is twice the fundamental ($\omega_{\mathrm{VIS}} = 3.0\,\mathrm{eV}$) to control PECD at the harmonic peaks [cf. Fig. 4(a)].

We consider the relative forward-backward anisotropy of photoelectron emission with respect to field propagation direction upon reversal of the XUV and IR polarization helicities. Both XUV and IR pulses copropagate along the laboratory-frame $z$ axis. The PECD is determined by the difference in the photoelectron angular distribution (PAD),

$$\mathrm{PECD}(\epsilon_k,\theta_{\boldsymbol{k}'},\phi_{\boldsymbol{k}'}) = \mathcal{N}_0^{-1}\left(\frac{d^2\sigma(\mathbf{e}_{\mathrm{XUV}},\mathbf{e}_{\mathrm{IR}})}{d\epsilon_k\,d\Omega_{\boldsymbol{k}'}} - \frac{d^2\sigma(\mathbf{e}'_{\mathrm{XUV}},\mathbf{e}'_{\mathrm{IR}})}{d\epsilon_k\,d\Omega_{\boldsymbol{k}'}}\right), \tag{2}$$

obtained with XUV and IR polarization configurations $(\mathbf{e}_{\mathrm{IR}},\mathbf{e}_{\mathrm{XUV}})$ and $(\mathbf{e}'_{\mathrm{IR}},\mathbf{e}'_{\mathrm{XUV}})$. Here, $\boldsymbol{k}'$ denotes the photoelectron momentum with energy $k^2/2$ and direction $\Omega_{\boldsymbol{k}'} = (\theta_{\boldsymbol{k}'},\phi_{\boldsymbol{k}'})$ in $\mathcal{R}'$ [39], and $\mathcal{N}_0 = \max[\mathrm{PAD}]$ is a normalization factor defined as the maximum intensity in the PAD [14].

In contrast to Ref. [15] operating in the multiphoton above-threshold ionization regime for the ionization step, we exploit here the single-photon character of the XUV-induced ionization to treat the photoionization dynamics perturbatively. Equation (1a) is then solved within the second-order time-dependent perturbative formalism of Refs. [21,40]. This allows us to describe XUV ionization and the ensuing IR-mediated transitions giving rise to two-photon interferences at the sidebands to the lowest-order approximation as well as to analytically perform the integration over all molecular orientations. The differential photoionization cross section then reads

$$\frac{d^2\sigma(\mathbf{e}_{\mathrm{XUV}},\mathbf{e}_{\mathrm{IR}})}{d\epsilon_k\,d\Omega_{\boldsymbol{k}'}} \approx \int\left|\alpha^{\boldsymbol{k}'(1)}_{i_0}(\gamma_\mathcal{R}) + \alpha^{\boldsymbol{k}'(2)}_{i_0}(\gamma_\mathcal{R})\right|^2 d^3\gamma_\mathcal{R}, \tag{3}$$

with $\alpha^{\boldsymbol{k}'(1,2)}_{i_0}(\gamma_\mathcal{R}) = \langle\Phi^{\boldsymbol{k}'}_{i_0}|\Psi^{N(1,2)}_{\gamma_\mathcal{R}}(t)\rangle$ the first, resp. second, order corrections for $t\to\infty$, and where $i_0$ labels the highest occupied molecular orbital.

The states $|\Phi_{i_0}^{\boldsymbol{k}'}\rangle$ consisting of particle-hole excitations to the continuum orbitals $\varphi_{\boldsymbol{k}'}^{-}(\boldsymbol{r})$ are constructed from the antisymmetrized product [41,42]

$$\Phi_{i_0}^{\boldsymbol{k}'}(\boldsymbol{r}_1,\ldots,\boldsymbol{r}_N) = \mathcal{A}_N\big[\varphi_{\boldsymbol{k}'}^{-}(\boldsymbol{r});\Phi_{i_0}(\boldsymbol{r}_1,\ldots,\boldsymbol{r}_{N-1})\big]. \quad (4)$$

$\Phi_{i_0}(\boldsymbol{r}_1,\ldots,\boldsymbol{r}_{N-1})$ is the ionic component with $\boldsymbol{r}_j$ denoting the position of the $j$th electron. $\varphi_{\boldsymbol{k}'}^{-}(\mathbf{r})$ is the photoelectron scattering wave function in $\mathcal{R}'$. In $\mathcal{R}$, $\varphi_{\boldsymbol{k}}^{-}(\mathbf{r})$ is a solution of the scattering problem [43],

$$\left[-\frac{\nabla^2}{2}-\frac{1}{r}+V(\boldsymbol{r})-\frac{k^2}{2}\right]\varphi_{\boldsymbol{k}}^{-}(\boldsymbol{r})=0, \quad (5a)$$

with $V(\boldsymbol{r})$ the short-range portion of the static-exchange potential [43]. The scattering states with momentum $\boldsymbol{k}'$ in the laboratory frame are obtained according to

$$\varphi_{\boldsymbol{k}'}^{-}(\boldsymbol{r}) = \sum_{\ell,m,m'} \varphi_{k,\ell,m}^{-}(\boldsymbol{r})\,\mathcal{D}_{m,m'}^{(\ell)\dagger}(\gamma_{\mathcal{R}})Y_{m'}^{\ell *}(\Omega_{\boldsymbol{k}'}), \quad (5b)$$

with $\varphi_{k,\ell,m}^{-} = \langle \ell, m|\varphi_{\boldsymbol{k}}^{-}(\boldsymbol{r})\rangle$. The theoretical challenge in describing continuum-electron interferometry stems from calculating matrix elements between continuum states. Some schemes use regularization [44]; here, we choose to converge the corresponding matrix elements with respect to the Gaussian basis. This approach may converge systematically and takes advantage of the fact that the perturbed wave functions are semi-localized due to operation by the dipole (or other interaction) operator $\hat{\mu}$,

$$\psi^{(k)}(t) = (-i)^k \int_{t>t_1\ldots>t_k>t_0} e^{-i\hat{H}_0(t-t_1)}\,\hat{\mu}\,e^{-i\hat{H}_0(t_1-t_2)} \times\cdots\hat{\mu}\,e^{-i\hat{H}_0(t_k-t_0)}\,\psi(t_0)\,dt_1\cdots dt_k. \quad (6)$$

While each operation with $\hat{\mu}$ extends the range of the function, it is still local and representable by Gaussian functions, so long as they are converged. Calculations of occupied and unoccupied Hartree-Fock orbitals of the equilibrium geometry were obtained using the `MOLPRO` program package [45,46] using the augmented correlation consistent basis set `aug-cc-pVQZ` [47]. Transition matrix elements to scattering states were obtained with the `ePolyScat` program package [48–50].

Starting with the usual RABBITT scheme depicted in Fig. 1(a), we first investigate the influence of the IR-driven continuum transitions on the forward-backward PECD shown in Fig. 1, where $\theta_{\boldsymbol{k}'}$ describes the angle between the photoelectron direction of emission and the field propagation axis in the $(\hat{k}'_x,\hat{k}'_z)$ plane. The XUV pulse is defined by a synchronous frequency comb of odd-order harmonics $\omega_{11}$, $\omega_{13}$, and $\omega_{15}$ circularly polarized in the $x$, $y$ plane, as indicated in Fig. 1(a). Each harmonic is represented by a Fourier-limited pulse with intensity of $10^{11}\,\mathrm{W/cm^2}$, FWHM of 10 fs, and flat spectral phase ($\tau_n=\tau_{n+1}=0$). The IR field frequency ($\omega_{\mathrm{IR}}=\omega_0$) is fixed. The IR amplitude, FHWM, and delay with respect to the XUV comb are, in a first stage, scanned or optimized to obtain the maximum forward-backward anisotropy in the $(\hat{k}'_x,\hat{k}'_z)$ plane. No optimization over spectral components is carried out. Note that by taking the fundamental $\omega_0=1.5\,\mathrm{eV}$, XUV inner-shell and IR multiphoton contributions to the photoelectron spectra at the harmonic peaks $\mathcal{H}_{2n+1}$ and sidebands $\mathcal{S}_{2n}$ of interest are avoided, while simultaneously placing IR excitation of vibrational modes far from resonance [51].

In the absence of the IR component, the XUV comb induces the PECD and PAD shown in upper and lower hemispheres of Fig. 1(b), exploiting their symmetry with respect to the field propagation axis. The PAD in Fig. 1(b) shows that the ionization probability is enhanced in the direction perpendicular to the light propagation axis. The XUV ionization results in a maximum PECD of 2% at a photoelectron kinetic energy of 6 eV, corresponding to single-photon ionization driven by the harmonic $\omega_{11}$ in the XUV comb. The maximum forward-backward anisotropy induced by the XUV comb alone [Fig. 1(b)] is parallel to the light propagation direction, which is typical in the single-photon regime without any quantum pathway interference. The presence of the IR pulse induces two-photon interferences at the sidebands [cf. Fig. 1(a)]. The relative phase of these pathways can be controlled by means of the XUV-IR relative delay. Figure 1(c) shows the PECD and PAD obtained by XUV ionization in the presence of an IR field with optimized intensity of $1.26\times10^{12}\,\mathrm{W/cm^2}$ and delay of $+0.92$ fs with respect to the XUV comb of Fig. 1(b). In this case, the PECD reaches 10% at the sideband $\mathcal{S}_{14}$ (10.5 eV). It corresponds to the photoelectron kinetic energy where IR-mediated interferences between the photoelectron components ionized by the harmonics $\omega_{13}$ and $\omega_{15}$ take place.

Remarkably, XUV ionization in the presence of the optimized IR pulse vanishes at the harmonic peaks, indicating a highly efficient population transfer dynamics from the harmonics $\mathcal{H}_{2q+1}$ to the sidebands $\mathcal{S}_{2q}$ induced by the delay-optimized IR pulse. The fact that ionization is maximized at the sideband $\mathcal{S}_{12}$ (7.5 eV) while PECD reaches its maximum at 10.5 eV $\mathcal{S}_{14}$ can be attributed to kinetic effects, since the PECD is normalized with respect to the PAD peak intensity, in this case the PAD peak intensity at 7.5 eV.

The enhancement in the PECD due to the presence of the IR pulse, largest at the sideband $\mathcal{S}_{14}$ (10.5 eV) [cf. Fig. 1(c)], is obtained with circular polarization of both XUV and IR pulses. The corresponding polarization reversal is indicated by the red (IR) and blue (XUV) arrows in Fig. 1(c). Removing the IR field and scanning the XUV frequency to promote single-photon XUV ionization within the energy range of interest (6–12 eV), in particular at the sidebands (4.5, 7.5, and 10.5 eV), result in a significantly smaller PECD effect, of only 3% at 6.25 eV (cf. the Supplemental Material [52]). This procedure allows us to exclude kinetic energy effects and confirms an interference effect as the main driver for PECD enhancement.

Rather than removing the IR field and thus the interferences, we can also perform the reversal of the circular polarization in only one of the fields [52]. The strongest PECD values, however, are obtained under polarization reversal of both the XUV and IR fields. This suggests that chiral-sensitive contributions from bound-continuum and continuum-continuum transitions are combined to enhance the overall PECD, as we discuss in more detail below. Finally, the different angular dependencies at the sidebands in Fig. 1(c) are also explained by the interferences driven by the IR at the sidebands $\mathcal{S}_{2n}$, as illustrated in Fig. 1(a). In fact, while in one-photon ionization the PECD at the harmonics arises from

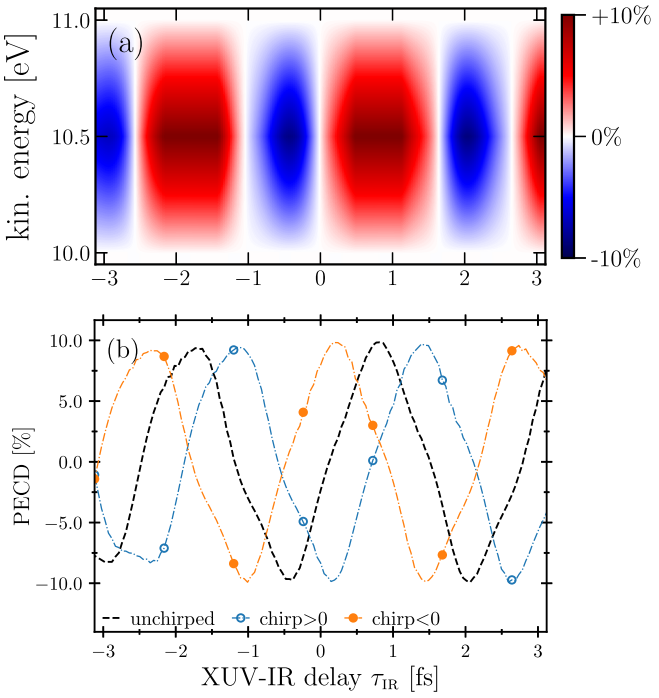


FIG. 2. Robustness of RABBITT-PECD: (a) PECD trace along the sideband $\mathcal{S}_{14}$ of Fig. 1(a) as a function of the XUV-IR time delay at the emission direction $\theta_{k'} = 0°$ obtained with identical circular polarization states for the XUV and IR fields with polarization reversal as in Fig. 1(c). (b) Influence of the XUV comb delay dispersion on the sideband $\mathcal{S}_{14}$: positive and negative chirps merely shift the PECD value with respect to the unchirped case.

unequal contributions of continuum states with negative and positive odd magnetic quantum numbers $m$ [2], the IR field induces interferences between the amplitude distributions of two consecutive harmonics that mix their odd and even $m$ at a given sideband. Since the distribution of odd and even $m$ at the harmonics is energy dependent, such a mixing explains the difference in the angular distributions at the two sidebands in Fig. 1(c).

The extent to which the interferences are controlled by the relative delay between the IR and XUV fields is investigated in Fig. 2(a), showing the PECD trace centered around the sideband $\mathcal{S}_{14}$ of Fig. 1(a), at 10.5 eV, for the IR- and XUV-reversed polarization configurations displayed in Fig. 1(c). An oscillating behavior of the PECD as a function of the XUV-IR time delay is observed with alternating PECD sign. For long IR durations (20 fs), the PECD exhibit cosine-type oscillations, which is expected from an IR field of constant amplitude as in RABBITT [27,28] where the much shorter XUV field is contained within half of the IR period. As the IR duration decreases toward that of each component of the XUV comb (10 fs), the PECD still oscillates as a function of the XUV-IR delay but the oscillations deviate from a pure cosine like behavior, resulting in the oscillation patten shown in Fig. 2(b); see Ref. [52] for more details or Ref. [24] for CEP effects in forward-backward PECD. The maximum achievable PECD increases for shorter IR durations and reaches a plateau as a function of the ratio of IR to XUV intensities (which occurs at a few percent). This plateau corresponds to the case where the photoelectron signal at the sidebands overtakes the photoelectron peak intensity initially at the harmonics in the absence of the IR. In all cases, the PECD amplitude exhibits an oscillatory behavior as a function of the relative XUV-IR delay $\tau_{IR}$. This is of particular interest for PECD enhancement as the tedious task of pulse shaping for spectral phase optimization reduces to a scanning of the relative XUV-IR time delay as the maximum PECD magnitude is a periodic function of the delay. The PECD in Fig. 2(a) was obtained by assuming a flat spectral phase for the XUV comb, i.e., unchirped XUV harmonics. However, the RABBITT technique has revealed a quadratic spectral phase for the plateau of high harmonic generation [31,37,38,53,54]. This has been interpreted as a temporal dispersion in the emission time of the group delay associated with each harmonic $\omega_{2q+1}$ [37,38]. Consequently, the various XUV frequency components defining the comb are linearly delayed in time [37]. In Fig. 2(b), we investigate the effect of such delay dispersion on the PECD signal. In detail, a positive chirp, corresponding to lower XUV harmonics preceding the higher ones, introduces a shift of the PECD peaks toward positive XUV-IR time delays (blue line with empty circles) compared to the unchirped case (dotted black line). Conversely, a negative chirp results in a shift toward negative time delays (orange line with full circles). For a fixed delay, dispersion effects inherent to the high-order harmonic generation process may significantly affect the PECD strength. Remarkably, the chirped and unchirped XUV combs generate just delayed versions of the time-resolved PECD. This points to the robustness of the proposed interferometric scheme: If the XUV delay dispersion merely introduces a shift in the PECD oscillations, for an unknown chirp, the maximum achievable PECD can simply be retrieved by scanning the XUV-IR time delay (cf. Fig. 2(b)].

Modifying the polarization configurations allows us to extract even more information from the interferometric scheme. To this end, we reconsider the two-photon excitation pathways shown in Fig. 1(a), but unlike in Fig. 1(c), we use chiral-sensitive circular polarization in only one of the fields. In Fig. 3(a), with linearly polarized IR and circularly polarized XUV comb with left/right polarization reversal for the XUV field only, the forward-backward PECD originates from XUV-driven bound-continuum transitions only, whereas the continuum-continuum transitions driven by the IR field are not chiral-sensitive. As before, the interferences can be controlled by the XUV-IR delay, which for this choice of polarizations results in a maximum PECD of 8%, at a photoelectron kinetic energy of 10.5 eV [cf. Fig. 3(a)].

The difference between 8% in Fig. 3(a) and the 10% observed in Fig. 1(c) may be attributed to chiral effects in the continuum. To directly probe the chirality of the continuum states, we show in Fig. 3(b) the forward-backward PECD for fixed linearly polarized XUV comb and circularly polarized IR field with corresponding left-right polarization reversal. A maximum PECD of 2% is found at a photoelectron energy of 10.5 eV. The PECD shown in Fig. 3(b) is exclusively due to the continuum-continuum transitions since for linearly polarized XUV fields, bound-continuum transitions do not contribute to the PECD [2].

Finally, we modify the standard RABBITT scheme depicted in Fig. 1(a) to promote interferences between

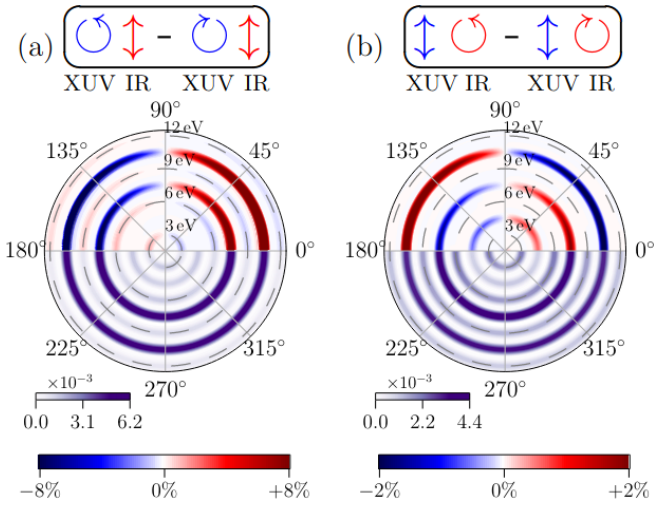


FIG. 3. Disentangling bound and continuum contributions to RABBITT-PECD by choice of the polarization configurations: (a) PECD (upper hemisphere) and PAD (lower hemisphere) obtained with XUV (circularly polarized in the $x, y$ plane) and IR (linearly polarized along the $y$ axis) pulses. PAD corresponds to the circularly left polarized XUV and linear IR field. (b) Same as panel (a) but with linearly polarized XUV (along $y$ axis) and circularly polarized IR ($x, y$ plane) pulses. In panel (b), PAD corresponds to the linearly polarized XUV and circularly left polarized IR. Shown are the maximum PECD obtained with their respective optimal time delays. Dotted gray lines indicate the harmonic peak $\mathcal{H}_{2q+1}$.

harmonics separated by $\omega_{\mathrm{VIS}} = 2\omega_{\mathrm{IR}} = 3.0\,\mathrm{eV}$, as indicated in Fig. 4(a). Optimizing the visible pulse parameters (amplitude, FWHM, time delay) while keeping those of the XUV as in Fig. 1 and with the relative polarization configuration

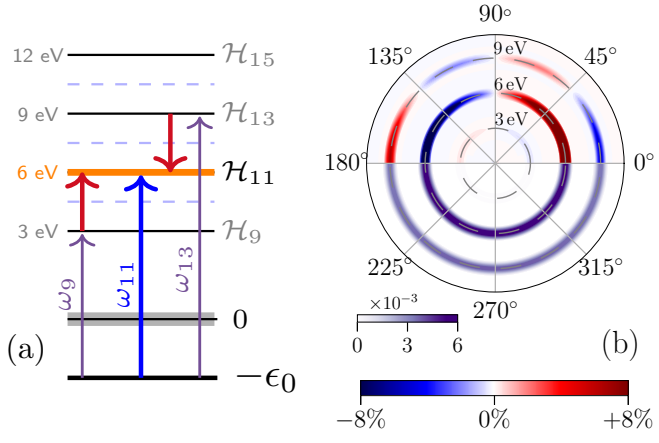


FIG. 4. (a) Modified RABBITT scheme for probing the kinetic energy dependence of PECD: Replacing the IR pulse by a visible field (with $\omega_{\mathrm{VIS}} = 2\omega_0$) results in interferences between even- and odd-parity pathways and controls PECD at the harmonic peaks instead of the sidebands. (b) Corresponding PECD (upper hemisphere) and PAD (lower hemisphere). PAD corresponds to the corotating circularly left polarized XUV and IR fields. PECD is to be compared to PECD without interference at the harmonic peaks [Fig. 1(b)] and to interference-enhanced PECD at the sidebands [Fig. 1(c)].

of Fig. 1(c), we obtain a maximum PECD of about 8% at a photoelectron kinetic energy of 6 eV, shown in Fig. 4(b). Analogously to Fig. 2(b), the magnitude of PECD oscillates as a function of the VIS-to-XUV time delay. The maximum PECD of 8% at 6 eV in Fig. 4(b) (upper hemisphere) has to be compared to the PECD of 2% at 6 eV obtained with the XUV alone shown in Fig. 1(b). The significant enhancement in PECD compared to Fig. 1(b) can be attributed to the interfering pathways $\omega_9 + 2\omega_{\mathrm{IR}}$ and $\omega_{13} - 2\omega_{\mathrm{IR}}$ depicted by the violet and red arrows in Fig. 4(a), which are absent in Fig. 1(b). In fact, the single-photon ionization pathway represented by $\omega_{11}$ in Fig. 4(a) plays a minor role in the PECD enhancement: removing $\omega_{11}$ from the XUV comb results in maximum PECD of 6%. The main contribution to the PECD enhancement observed in Fig. 4 can thus be attributed to a two-photon pathway interference effect, determined by the pathways $\omega_9 + 2\omega_{\mathrm{IR}}$ and $\omega_{13} - 2\omega_{\mathrm{IR}}$ interfering at 6 eV.

Replacing the IR field ($\omega_0 = 1.5$ eV) that maximizes the PECD at the sidebands in Fig. 1(c) with a visible field ($\omega_0 = 3.0$ eV) as in Fig. 4 allows us to probe and exploit kinetic energy dependence effects. Both two-photon interferometric approaches discussed here, i.e., standard and modified RABBITT schemes, result in an overall enhancement of the PECD compared to the XUV-only case. This attests to the ability of two-photon quantum pathway interferences to enhance PECD across the kinetic energy spectrum by exploiting continuum-continuum transitions with a minimum number of control parameters and offers a complementary control protocol to schemes based on bound-state one- and two-photon quantum interference.

In conclusion, using CHBrClF as a chiral prototype, we have identified a robust scheme for the coherent control of PECD in randomly oriented chiral molecules. It is based on two-photon quantum pathway interference where control is achieved simply by varying the XUV-IR time delay. This is in striking contrast to multicolor phase control schemes [21] that require pulse shaping techniques that, while within experimental reach, are not yet practically accessible as well as the accurate prediction of electronically excited states, which is out of reach even for the most advanced *ab initio* theories. At the same time, we have shown that the control is robust since the XUV comb delay dispersion simply introduces a shift in the PECD oscillations as a function of the XUV-IR time delay but does not affect the maximum PECD amplitude. Thus, effects of the spectral properties of the XUV train on the PECD can be compensated by adjusting the relative delay between the IR and XUV combs. We have also shown that changing polarizations of the XUV and IR pulses probes individual contributions of bound and continuum states to the PECD in a spectroscopic manner. Experimental verification of RABBITT-PECD would confirm that PECD is largely due to the chiral potential experienced by the bound state electrons, while continuum-state transitions contribute to a lesser extent. The continuum states, however, are critical to enhance PECD via interferences promoted by the IR field. Our work opens the way for robust coherent control of PECD as a practical tool to answer questions such as what determines the maximal value of a chiral observable or how does the chiral potential manifest itself in experimentally accessible quantities.

We acknowledge Chi-Hong Yuen for his contribution to implementing part of the code used in this work. The computing for this project was performed on the Beocat Research Cluster at Kansas State University, which is funded in part by NSF Grants No. CNS-1006860, No. EPS-1006860, No. EPS-0919443, No. ACI-1440548, No. CHE-1726332, and No. NIH P20GM113109, and used resources of the National Energy Research Scientific Computing Center (NERSC), a U.S. Department of Energy Office of Science User Facility operated under Contract No. DE-AC02-05CH11231 using NERSC Award No. BES-ERCAP0024357. C.A. and L.G. were supported by the Chemical Sciences, Geosciences, and Biosciences Division, Office of Basic Energy Sciences, Office of Science, U.S. Department of Energy, under Grant No. DE-SC0022105. C.A. also acknowledges NSF Grant No. 2244539 for additional support during the summer of 2023. A.B. and C.P.K. acknowledge financial support from the Deutsche Forschungsgemeinschaft (CRC 1319).

*Data Availability.* Some of the data that support the findings of this article are openly available in Ref. [52] in the form of input parameters for the electronic structure and scattering calculations obtained from publicly available program packages. Some of the data that support the findings of the article are not publicly available because they contain commercially sensitive information. The data are available upon reasonable request from the authors.

[1] A. D. McNaught and A. D. McNaught, *Compendium of Chemical Terminology* (Blackwell Science, Oxford, 1997), Vol. 1669.

[2] B. Ritchie, Theory of the angular distribution of photoelectrons ejected from optically active molecules and molecular negative ions, Phys. Rev. A **13**, 1411 (1976).

[3] C. Lux, M. Wollenhaupt, T. Bolze, Q. Liang, J. Köhler, C. Sarpe, and T. Baumert, Circular dichroism in the photoelectron angular distributions of camphor and fenchone from multiphoton ionization with femtosecond laser pulses, Angew. Chem. Int. Ed. **51**, 5001 (2012).

[4] C. Lux, M. Wollenhaupt, C. Sarpe, and T. Baumert, Photoelectron circular dichroism of bicyclic ketones from multiphoton ionization with femtosecond laser pulses, ChemPhysChem **16**, 115 (2015).

[5] C. Lux, A. Senftleben, C. Sarpe, M. Wollenhaupt, and T. Baumert, Photoelectron circular dichroism observed in the above-threshold ionization signal from chiral molecules with femtosecond laser pulses, J. Phys. B: At. Mol. Opt. Phys. **49**, 02LT01 (2016).

[6] A. Kastner, C. Lux, T. Ring, S. Züllighoven, C. Sarpe, A. Senftleben, and T. Baumert, Enantiomeric excess sensitivity to below one percent by using femtosecond photoelectron circular dichroism, ChemPhysChem **17**, 1119 (2016).

[7] A. Kastner, T. Ring, B. C. Krüger, G. B. Park, T. Schäfer, A. Senftleben, and T. Baumert, Intermediate state dependence of the photoelectron circular dichroism of fenchone observed via femtosecond resonance-enhanced multi-photon ionization, J. Chem. Phys. **147**, 013926 (2017).

[8] C. S. Lehmann, N. B. Ram, I. Powis, and M. H. M. Janssen, Imaging photoelectron circular dichroism of chiral molecules by femtosecond multiphoton coincidence detection, J. Chem. Phys. **139**, 234307 (2013).

[9] M. H. M. Janssen and I. Powis, Detecting chirality in molecules by imaging photoelectron circular dichroism, Phys. Chem. Chem. Phys. **16**, 856 (2014).

[10] M. M. R. Fanood, N. B. Ram, C. S. Lehmann, I. Powis, and M. H. M. Janssen, Enantiomer-specific analysis of multicomponent mixtures by correlated electron imaging–ion mass spectrometry, Nat. Commun. **6**, 7511 (2015).

[11] M. M. R. Fanood, M. H. M. Janssen, and I. Powis, Enantioselective femtosecond laser photoionization spectrometry of limonene using photoelectron circular dichroism, Phys. Chem. Chem. Phys. **17**, 8614 (2015).

[12] R. Cireasa, A. E. Boguslavskiy, B. Pons, M. C. H. Wong, D. Descamps, S. Petit, H. Ruf, N. Thiré, A. Ferré, J. Suarez, J. Higuet, B. E. Schmidt, A. F. Alharbi, F. Légaré, V. Blanchet, B. Fabre, S. Patchkovskii, O. Smirnova, Y. Mairesse, and V. R. Bhardwaj, Probing molecular chirality on a sub-femtosecond timescale, Nat. Phys. **11**, 654 (2015).

[13] A. Comby, S. Beaulieu, M. Boggio-Pasqua, D. Descamps, F. Légaré, L. Nahon, S. Petit, B. Pons, B. Fabre, Y. Mairesse, and V. Blanchet, Relaxation dynamics in photoexcited chiral molecules studied by time-resolved photoelectron circular dichroism: Toward chiral femtochemistry, J. Phys. Chem. Lett. **7**, 4514 (2016).

[14] S. Beaulieu, A. Comby, B. Fabre, D. Descamps, A. Ferré, G. Garcia, R. Géneaux, F. Légaré, L. Nahon, S. Petit, T. Ruchon, B. Pons, V. Blanchet, and Y. Mairesse, Probing ultrafast dynamics of chiral molecules using time-resolved photoelectron circular dichroism, Faraday Discuss. **194**, 325 (2016).

[15] S. Beaulieu, A. Comby, A. Clergerie, J. Caillat, D. Descamps, N. Dudovich, B. Fabre, R. Géneaux, F. Légaré, S. Petit, B. Pons, G. Porat, T. Ruchon, R. Taïeb, V. Blanchet, and Y. Mairesse, Attosecond-resolved photoionization of chiral molecules, Science **358**, 1288 (2017).

[16] S. Beaulieu, A. Comby, D. Descamps, B. Fabre, G. A. Garcia, R. Géneaux, A. G. Harvey, F. Légaré, Z. Masin, L. Nahon, A. F. Ordonez, S. Petit, B. Pons, Y. Mairesse, O. Smirnova, and V. Blanchet, Photoexcitation circular dichroism in chiral molecules, Nat. Phys. **14**, 484 (2018).

[17] J. Miles, D. Fernandes, A. Young, C. Bond, S. Crane, O. Ghafur, D. Townsend, J. Sá, and J. Greenwood, A new technique for probing chirality via photoelectron circular dichroism, Anal. Chim. Acta **984**, 134 (2017).

[18] N. Böwering, T. Lischke, B. Schmidtke, N. Müller, T. Khalil, and U. Heinzmann, Asymmetry in photoelectron emission from chiral molecules induced by circularly polarized light, Phys. Rev. Lett. **86**, 1187 (2001).

[19] U. Hergenhahn, E. E. Rennie, O. Kugeler, S. Marburger, T. Lischke, I. Powis, and G. Garcia, Photoelectron circular dichroism in core level ionization of randomly oriented pure enantiomers of the chiral molecule camphor, J. Chem. Phys. **120**, 4553 (2004).

[20] D. S. Tikhonov, A. Blech, M. Leibscher, L. Greenman, M. Schnell, and C. P. Koch, Pump-probe spectroscopy of chiral vibrational dynamics, Sci. Adv. **8**, eade0311 (2022).

[21] R. E. Goetz, C. P. Koch, and L. Greenman, Quantum control of photoelectron circular dichroism, Phys. Rev. Lett. **122**, 013204 (2019).

[22] V. Hanus, S. Kangaparambil, M. Richter, L. Haßfurth, M. Dorner-Kirchner, G. G. Paulus, X. Xie, A. Baltuška, S. Gräfe, and M. Zeiler, Carrier envelope phase sensitivity of photoelectron circular dichroism, Phys. Chem. Chem. Phys. **25**, 4656 (2023).

[23] P. V. Demekhin, A. N. Artemyev, A. Kastner, and T. Baumert, Photoelectron circular dichroism with two overlapping laser pulses of carrier frequencies $\omega$ and $2\omega$ linearly polarized in two mutually orthogonal directions, Phys. Rev. Lett. **121**, 253201 (2018).

[24] S. Rozen, A. Comby, E. Bloch, S. Beauvarlet, D. Descamps, B. Fabre, S. Petit, V. Blanchet, B. Pons, N. Dudovich, and Y. Mairesse, Controlling subcycle optical chirality in the photoionization of chiral molecules, Phys. Rev. X **9**, 031004 (2019).

[25] G. Hartmann, M. Ilchen, P. Schmidt, C. Küstner-Wetekam, C. Ozga, F. Scholz, J. Buck, F. Trinter, J. Viefhaus, A. Ehresmann, M. S. Schöffler, A. Knie, and P. V. Demekhin, Recovery of high-energy photoelectron circular dichroism through fano interference, Phys. Rev. Lett. **123**, 043202 (2019).

[26] M. W. Heger and D. M. Reich, Tracking chirality in photoelectron circular dichroism, Phys. Rev. Res. **7**, L012047 (2025).

[27] P. M. Paul, E. S. Toma, P. Breger, G. Mullot, F. Augé, P. Balcou, H. G. Muller, and P. Agostini, Observation of a train of attosecond pulses from high harmonic generation, Science **292**, 1689 (2001).

[28] H. Muller, Reconstruction of attosecond harmonic beating by interference of two-photon transitions, Appl. Phys. B **74**, s17 (2002).

[29] T. Mazza, M. Ilchen, A. J. Rafipoor, C. Callegari, P. Finetti, O. Plekan, K. C. Prince, R. Richter, M. Danailov, A. Demidovich *et al.*, Determining the polarization state of an extreme ultraviolet free-electron laser beam using atomic circular dichroism, Nat. Commun. **5**, 3648 (2014).

[30] S. Donsa, N. Douguet, J. Burgdörfer, I. Březinová, and L. Argenti, Circular holographic ionization-phase meter, Phys. Rev. Lett. **123**, 133203 (2019).

[31] K. Klünder, J. M. Dahlström, M. Gisselbrecht, T. Fordell, M. Swoboda, D. Guénot, P. Johnsson, J. Caillat, J. Mauritsson, A. Maquet, R. Taïeb, and A. L'Huillier, Probing single-photon ionization on the attosecond time scale, Phys. Rev. Lett. **106**, 143002 (2011).

[32] M. Han, J.-B. Ji, T. Balčiūnas, K. Ueda, and H. J. Wörner, Attosecond circular-dichroism chronoscopy of electron vortices, Nat. Phys. **19**, 230 (2023).

[33] M. Han, J.-B. Ji, K. Ueda, and H. J. Wörner, Attosecond metrology in circular polarization, Optica **10**, 1044 (2023).

[34] M. D. J. Waters, N. Ladda, A. Senftleben, V. Svoboda, M. Belozertsev, T. Baumert, and H. J. Wörner, Ground-state photoelectron circular dichroism of methyl *p*-tolyl sulfoxide by single-photon ionisation from a table-top source, ChemPhysChem **23**, e202200575 (2022).

[35] M. Pitzer, M. Kunitski, A. S. Johnson, T. Jahnke, H. Sann, F. Sturm, L. P. H. Schmidt, H. Schmidt-Böcking, R. Dörner, J. Stohner, J. Kiedrowski, M. Reggelin, S. Marquardt, A. Schießer, R. Berger, and M. S. Schöffler, Direct determination of absolute molecular stereochemistry in gas phase by Coulomb explosion imaging, Science **341**, 1096 (2013).

[36] K. Fehre, S. Eckart, M. Kunitski, C. Janke, D. Trabert, M. Hofmann, J. Rist, M. Weller, A. Hartung, L. P. H. Schmidt, T. Jahnke, H. Braun, T. Baumert, J. Stohner, P. V. Demekhin, M. S. Schöffler, and R. Dörner, Strong differential photoion circular dichroism in strong-field ionization of chiral molecules, Phys. Rev. Lett. **126**, 083201 (2021).

[37] S. Kazamias and P. Balcou, Intrinsic chirp of attosecond pulses: Single-atom model versus experiment, Phys. Rev. A **69**, 063416 (2004).

[38] Y. Mairesse, A. de Bohan, L. J. Frasinski, H. Merdji, L. C. Dinu, P. Monchicourt, P. Breger, M. Kovačev, R. Taïeb, B. Carré, H. G. Muller, P. Agostini, and P. Salières, Attosecond synchronization of high-harmonic soft x-rays, Science **302**, 1540 (2003).

[39] PECD is given at fixed $\phi_{k'} = \pi/2$; see, e.g., Refs. [21,23,40] for a detailed description of the detection geometry.

[40] R. E. Goetz, C. P. Koch, and L. Greenman, Perfect control of photoelectron anisotropy for randomly oriented ensembles of molecules by XUV REMPI and polarization shaping, J. Chem. Phys. **151**, 074106 (2019).

[41] C. W. McCurdy, D. A. Horner, and T. N. Rescigno, Practical calculation of amplitudes for electron-impact ionization, Phys. Rev. A **63**, 022711 (2001).

[42] M. Baertschy, T. N. Rescigno, and C. W. McCurdy, Accurate amplitudes for electron-impact ionization, Phys. Rev. A **64**, 022709 (2001).

[43] R. R. Lucchese, G. Raseev, and V. McKoy, Studies of differential and total photoionization cross sections of molecular nitrogen, Phys. Rev. A **25**, 2572 (1982).

[44] N. Douguet, B. I. Schneider, and L. Argenti, Application of the complex Kohn variational method to attosecond spectroscopy, Phys. Rev. A **98**, 023403 (2018).

[45] H.-J. Werner, P. J. Knowles, F. R. Manby, J. A. Black, K. Doll, A. Heßelmann, D. Kats, A. Köhn, T. Korona, D. A. Kreplin, Q. Ma, T. F. Miller, III, A. Mitrushchenkov, K. A. Peterson, I. Polyak, G. Rauhut, and M. Sibaev, The Molpro quantum chemistry package, J. Chem. Phys. **152**, 144107 (2020).

[46] H.-J. Werner, P. J. Knowles, G. Knizia, F. R. Manby, and M. Schütz, Molpro: a general-purpose quantum chemistry program package, WIREs Comput. Mol. Sci. **2**, 242 (2012).

[47] R. A. Kendall, T. H. Dunning, and R. J. Harrison, Electron affinities of the first-row atoms revisited. Systematic basis sets and wave functions, J. Chem. Phys. **96**, 6796 (1992).

[48] F. A. Gianturco, R. R. Lucchese, and N. Sanna, Calculation of low-energy elastic cross sections for electron-$CF_4$ scattering, J. Chem. Phys. **100**, 6464 (1994).

[49] A. P. P. Natalense and R. R. Lucchese, Cross section and asymmetry parameter calculation for sulfur 1s photoionization of $SF_6$, J. Chem. Phys. **111**, 5344 (1999).

[50] L. Greenman, R. R. Lucchese, and C. W. McCurdy, Variational treatment of electron–polyatomic-molecule scattering calculations using adaptive overset grids, Phys. Rev. A **96**, 052706 (2017).

[51] M. Diem and D. F. Burow, Vibrational spectra and normal coordinate analysis of bromochlorofluoromethane, J. Chem. Phys. **64**, 5179 (1976).

[52] See Supplemental Material at http://link.aps.org/supplemental/10.1103/8f7h-6nfc for detailed information on convergence test calculations, sensitivity of the photoelectron circular dichroism on the full width at half maximum (FWHM) of the IR field, and input file parameters for the electronic structure and scattering calculations.

[53] K. Varjú, Y. Mairesse, P. Agostini, P. Breger, B. Carré, L. J. Frasinski, E. Gustafsson, P. Johnsson, J. Mauritsson, H. Merdji, P. Monchicourt, A. L'Huillier, and P. Salières, Reconstruction of attosecond pulse trains using an adiabatic phase expansion, Phys. Rev. Lett. **95**, 243901 (2005).

[54] M. Isinger, D. Busto, S. Mikaelsson, S. Zhong, C. Guo, P. Salières, C. Arnold, A. L'Huillier, and M. Gisselbrecht, Accuracy and precision of the RABBIT technique, Philos. Trans. R. Soc. A **377**, 20170475 (2019).